

Cite this: *Nanoscale Adv.*, 2022, 4, 590

# Colloidal 2D PbSe nanoplatelets with efficient emission reaching the telecom O-, E- and S-band†

Lars F. Klepzig,<sup>ab</sup> Leon Biesterfeld,<sup>ab</sup> Michel Romain,<sup>a</sup> André Niebur,<sup>ab</sup>  
Anja Schlosser,<sup>ac</sup> Jens Hübner<sup>cd</sup> and Jannika Lauth<sup>abc</sup>

Colloidal two-dimensional (2D) lead chalcogenide nanoplatelets (NPLs) represent highly interesting materials for near- and short wave-infrared applications including innovative glass fiber optics exhibiting negligible attenuation. In this work, we demonstrate a direct synthesis route for 2D PbSe NPLs with cubic rock salt crystal structure at low reaction temperatures of 0 °C and room temperature. A lateral size tuning of the PbSe NPLs by controlling the temperature and by adding small amounts of octylamine to the reaction leads to excitonic absorption features in the range of 1.55–1.24 eV (800–1000 nm) and narrow photoluminescence (PL) reaching the telecom O-, E- and S-band (1.38–0.86 eV, 900–1450 nm). The PL quantum yield of the as-synthesized PbSe NPLs is more than doubled by a postsynthetic treatment with CdCl<sub>2</sub> (e.g. from 14.7% to 37.4% for NPLs emitting at 980 nm with a FWHM of 214 meV). An analysis of the slightly asymmetric PL line shape of the PbSe NPLs and their characterization by ultrafast transient absorption and time-resolved PL spectroscopy reveal a surface trap related PL contribution which is successfully reduced by the CdCl<sub>2</sub> treatment from 40% down to 15%. Our results open up new pathways for a direct synthesis and straightforward incorporation of colloidal PbSe NPLs as efficient infrared emitters at technologically relevant telecom wavelengths.

Received 22nd September 2021  
Accepted 14th December 2021

DOI: 10.1039/d1na00704a

rsc.li/nanoscale-advances

## Introduction

Atomically-thin quasi-two-dimensional (2D) IV–VI semiconductors, especially lead chalcogenide nanosheets (NSs) and nanoplatelets (NPLs), have attracted significant interest due to their promising optoelectronic properties covering the near-infrared (NIR) and short-wave-infrared (SWIR) wavelength range of the electromagnetic spectrum.<sup>1–3</sup> 2D NSs and NPLs belong to the same category with NPLs typically showing lateral sizes <100 nm. The materials exhibit broadly tunable absorption and photoluminescence (PL) properties, which are controlled mainly by their quantum-confined thickness and provide access to the spectral windows needed in biological imaging or fiber optics.<sup>4–6</sup> 2D lead chalcogenide NSs for example show photophysics different from their spherical nanocrystal (NC) counterparts such as strong Rashba spin–orbit coupling,<sup>7</sup>

even more efficient carrier multiplication,<sup>8</sup> and high charge carrier mobility.<sup>9,10</sup> This allows for their use as active optical components for field effect transistors (FETs),<sup>11</sup> light-emitting diodes (LEDs),<sup>12</sup> or solar cells.<sup>13,14</sup> Additionally, colloidal lead chalcogenides are highly interesting nanomaterials for deterministic single photon emission which is applied in photonic quantum technologies like quantum key distribution.<sup>15–18</sup>

However, synthetic access, especially to NPLs exhibiting seamlessly tunable and efficient NIR to SWIR PL is scarce. For example, Tenney *et al.* synthesized HgTe NPLs decorated with HgTe NCs that exhibited efficient PL with a quantum yield (QY) of >30% between 1000 and 1500 nm. The synthesis is elaborate, requiring a cation exchange from CdSe NPLs and a simultaneous ligand exchange.<sup>19</sup> A similar cation exchange approach from CdSe NPLs to PbSe NPLs has been described by Galle *et al.*<sup>20,21</sup> The starting CdSe NPLs show high brightness and narrow PL that is partly retained during the cation exchange.<sup>22</sup> Thin cation exchanged PbSe NPLs from 4 monolayer (ML) CdSe yielded a PLQY of 15% centered at 1330 nm, whereas the thickest PbSe NPLs of 6 ML exhibited a PLQY of 6% centered at 1545 nm.<sup>20</sup>

While straightforward and direct colloidal synthesis methods for PbS and PbSe NCs are well established, relatively few studies deal with the direct synthesis of strongly confined IV–VI semiconductor NPLs,<sup>2,23–28</sup> even less based on PbSe.<sup>3</sup> Recently, we have shown the synthesis of ultrathin PbS NPLs with enhanced NIR emission.<sup>29</sup>

<sup>a</sup>Institute of Physical Chemistry and Electrochemistry, Leibniz Universität Hannover, Callinstr. 3A, 30167 Hannover, Germany. E-mail: jannika.lauth@pci.uni-hannover.de

<sup>b</sup>Cluster of Excellence PhoenixD (Photonics, Optics, and Engineering – Innovation Across Disciplines), 30167 Hannover, Germany

<sup>c</sup>Laboratory of Nano and Quantum Engineering (LNQE), Leibniz Universität Hannover, Schneiderberg 39, 30167 Hannover, Germany

<sup>d</sup>Institute of Solid State Physics, Leibniz Universität Hannover, Appelstraße 2, 30167 Hannover, Germany

† Electronic supplementary information (ESI) available: Complementary results, including powder X-ray diffraction, energy dispersive X-ray spectroscopy, excitation spectroscopy. See DOI: 10.1039/d1na00704a



The synthesis of cubic 2D NSs and NPLs requires anisotropic crystal growth, which can be induced by different strategies including oriented attachment leading to symmetry breaking,<sup>1,3,30</sup> cation exchange,<sup>20,31</sup> templated growth,<sup>26,32,33</sup> and intrinsic instabilities leading to enhanced growth of the basal plane.<sup>34</sup>

Koh *et al.* describe the synthesis of thickness-controlled 2D PbSe NPLs by oriented attachment of PbSe NCs.<sup>3</sup> They find a crucial role of halide ions to be responsible for a 2D bridging of the NCs, whereas the thickness is controlled by the amount of PbI<sub>2</sub> added. While a tunable PL was achieved by controlling the NPL thickness, the measured PLQY of ~0.1% was rather low.

Here, we report the first direct synthesis of 2D PbSe NPLs with efficient broadband tunable infrared emission by using lead oleate and selenourea as precursors in a mixture of octylamine and oleic acid.<sup>35–37</sup> PbSe NPLs are synthesized at room temperature or below and exhibit distinct excitonic absorption features between 800–1000 nm (1.55–1.24 eV), while narrow PL is obtained at technologically relevant telecommunication wavelengths between 900–1450 nm (1.38–0.86) eV, reaching the O-, E- and S-band (0.98–0.91, 0.91–0.85 and 0.85–0.81 eV, resp.). By adjusting the reaction temperature and the amount of octylamine used for the synthesis, the optical properties of the NPLs are tuned by controlling their lateral size rather than their thickness. In a subsequent step, a postsynthetic surface treatment of the PbSe NPLs with CdCl<sub>2</sub> leads to a general doubling of the PLQY of PbSe NPLs (*e.g.*, from 14.7% to 37.4% for NPLs emitting at 980 nm), exceeding the best results for PbSe NPLs published so far.

## Experimental

### Chemicals

Octylamine (OcAm, 99.0%), oleic acid (HOA, ≥99%) and cadmium chloride (CdCl<sub>2</sub>, 99.99%) were purchased from Sigma-Aldrich/Merck. Selenourea (99.97%) and analytical grade hexane (99.99%, anhydrous) were purchased from Alfa Aesar. Ethanol (99.9%, extra dry) was purchased from Acros. Tetrachloroethylene (TCE, ≥99.9%, anhydrous) was purchased from Merck-Millipore. Octylamine was dried *via* freeze–pump–thawing for three times. All other reagents were used as received without further purification.

### Synthesis of the lead oleate precursor (Pb(OA)<sub>2</sub>)

The synthesis of lead oleate is based on a method described by Hendricks *et al.* and has been recently proven successful for the synthesis of 2D PbS NPLs.<sup>31,38</sup> Briefly, 5 g (22.4 mmol) lead oxide were stirred in 10 mL acetonitrile for 10 min at 0 °C. The solution turned clear after the addition of 0.35 mL (4.54 mmol) trifluoroacetic acid and 3.1 mL (22.3 mmol) trifluoroacetic anhydride and was allowed to reach room temperature. A separate solution of 14.2 mL (45.0 mmol) HOA, 7.1 mL (50.6 mmol) triethylamine and 90 mL isopropanol was prepared and added to the lead solution. The white precipitate was purified by recrystallization after refluxing at 80 °C for 10 min until a clear solution was obtained. The solution was stored in a freezer (–20

°C) for 19 h before being filtered and washed with methanol. The dried lead oleate was stored in a glovebox at –24 °C.

### Synthesis of the selenourea precursor

In a 9 mL vial, a mixture of 193 mg (1.57 mmol) selenourea, 2 mL (12 mmol) OcAm, 0.2 mL (0.7 mmol) HOA and 0.75 mL hexane was prepared. The mixture was stirred at 35 °C at least for 24 h until a clear dark-orange solution was obtained. The selenium precursor was used for up to five days.

### PbSe NPL synthesis

The synthesis of PbSe NPLs is based on a method by Manteiga Vázquez *et al.*<sup>29</sup> The precursor formation steps and the reaction were run under inert gas conditions either inside a glovebox or on a Schlenk apparatus. The syntheses at 0 °C were conducted using an ice bath. In a 9 mL vial, 182.5 mg (0.3 mmol) Pb(OA)<sub>2</sub> was dissolved in a mixture of 0.8 mL (4.9 mmol) OcAm, 0.4 mL (1.3 mmol) HOA and 1.2 mL (9.2 mmol) hexane. 250 μL of the Se-precursor solution was injected into the Pb-precursor solution rapidly under vigorous stirring, and was kept stirring for additional 10 min. The solution immediately changes from colorless to dark brown upon the selenium precursor addition. The precipitation of the PbSe NPLs is induced by the addition of 2 mL dry ethanol after which the reaction product is centrifuged at 6000 rpm for 10 min. Precipitated PbSe NPLs are redispersed in hexane and stored in a glovebox at –24 °C. The absorption and PL properties of the PbSe NPLs can be controlled *via* the amount of OcAm used for the Pb(OA)<sub>2</sub>-precursor and the reaction temperature.

### CdCl<sub>2</sub> treatment of the PbSe NPLs

For the postsynthetic CdCl<sub>2</sub> treatment of PbSe NPLs, 0.275 g (1.5 mmol) CdCl<sub>2</sub> were dissolved in a mixture of 13.5 mL (81.9 mmol) OcAm and 1.5 mL (4.7 mmol) HOA. 2.5 mL of this solution was added to the crude PbSe NPL product and stirred for additional 40 min at 0 °C. The precipitation and storage steps were performed as described above.

### Vis-NIR and PL spectroscopy

The samples for vis-NIR and PL spectroscopy were prepared by diluting the unprecipitated PbSe NPLs in TCE. Optical absorption spectra were acquired on a Cary 5000 spectrophotometer from Agilent Technologies. Steady-state PL spectra and lifetime measurements (multi-channel scaling, MCS) were measured using an Edinburgh FLS 1000 UV-Vis-NIR PL spectrometer. The optical characterization of NPL dispersions was carried out using quartz cuvettes with a path length of 10 mm. The steady-state PL was collected by exciting the samples at 500 nm (optical density < 0.2 at the excitation wavelength) with a xenon lamp and utilizing an InGaAs PMT detector. The PLQY was determined with an integrating sphere, measuring the scattering in the visible range with a 980 PMT and the PL in the NIR with the InGaAs detector of both a blank and the sample. The measured spectra were corrected for the difference in the detector sensitivities. The MCS measurements were carried out using



a picosecond pulsed diode laser (EPL) with a wavelength of 445.1 nm and a pulse width of 110 ps by Edinburgh Instruments.

### Powder X-ray diffraction (PXRD)

Powder X-ray diffraction patterns were measured in Bragg–Brentano geometry using a Bruker D8 Advance equipped with  $\text{CuK}_{\alpha 1}$  source operating at 40 kV and 30 mA. The samples were prepared by drop-casting a concentrated NPL solution onto a single silicon crystal sample holder.

### Transition electron microscopy (TEM)

TEM analysis was conducted using a FEI Tecnai G2 F20 transmission electron microscope equipped with a field emission gun operating at 200 kV. The NPL samples for TEM were prepared by drop casting a diluted solution onto a carbon coated copper grid (300 mesh) by Quantifoil.

### Energy-dispersive X-ray spectroscopy (EDXS)

The atomic ratios of the PbSe NPL samples were determined using a scanning electron microscope (SEM) and analyzed by EDXS by using the software Oxford Instruments INCA 3000. SEM analysis was carried out using a JEOL JSM 6700F equipped with a cold field emission gun electron source. The samples were prepared by drop-casting a concentrated NPL solution onto a single silicon crystal sample holder.

### Transient absorption spectroscopy (TAS)

Ultrafast broadband transient optical absorption spectroscopy was performed on a set-up similar as described in literature.<sup>29,39,40</sup> Briefly, a 100 fs laser pulse train from a Ti:sapphire amplifier system (Spectra-Physics, Spitfire ACE) centered at 800 nm is split (90 : 10) to generate a pump and a probe beam. A broadband white-light super continuum is generated by nonlinear processes inside a  $\text{CaF}_2$  or sapphire crystal (320–1600 nm, Ultrafast, Helios FIRE) with the 10% share of the fundamental. The arrival of the probe beam with respect to the pump beam is varied by using a delay stage with a range of up to 8 ns after photoexcitation. The pump beam photoexcitation energy is controlled by nonlinear frequency mixing in an optical parametric amplifier (OPA) system (TOPAS). The pump pulse is dumped after the photoexcitation of the sample, while the probe light is led to a fiber-coupled detector array.

For TA measurements PbSe NPL samples were diluted in TCE in 2 mm quartz cuvettes and kept under constant stirring to prevent photocharging.<sup>41</sup> The optical density of the samples at the photoexcitation wavelength was kept at values  $\leq 0.1$ .

## Results and discussion

### Tunable absorption and PL properties of PbSe NPLs

Fig. 1a and b shows the absorption and PL spectra of PbSe NPLs exhibiting excitonic absorption features in the range of 1.55–1.24 eV (800–1000 nm) as well as narrow PL between 1.38–0.86 eV (900–1450 nm, see Fig. S1†). Fig. 1c–f depicts the corresponding TEM images of the samples, with the average NPL

edge lengths given in each image (see Fig. S2† for associated size histograms). PbSe NPLs exhibit a slightly rectangular shape with an aspect ratio of 1 : 1.1 to 1.2, a lateral size deviation of 15% and cubic rock salt crystal structure determined by powder XRD (Fig. S3†). Additional TEM images of single NPLs lying on their edges reveal a thickness of  $0.8 \pm 0.1$  nm (Fig. S4†).

We find the influence on the lateral size of the PbSe NPLs strongly dependent on the reaction temperature and the amount of OcAm used for the synthesis. While a low reaction temperature (0 °C) and a low amount of OcAm present during reaction is favorable for the formation of smaller PbSe NPLs, an increase of the temperature (to room temperature) and/or of the amount of OcAm leads to larger lateral NPL sizes and a tunable red shift of their absorption and PL features (see Fig. 1b). An influence on the reaction kinetics, which are affected by the temperature and the strong interaction between the amine and the lead ions, likely leads to the observed spectral tunability.<sup>2,42</sup> For example, Buhro and co-workers used OcAm to dissolve  $\text{CdX}_2$  precursors at room temperature, forming  $(\text{CdSe})_{13}$  nanoclusters between amine double layers, which in turn yielded 2D nanobelts upon heating.<sup>32</sup> A similar soft template mechanism is assumed to be occurring in our case. Additionally, the interaction between OcAm and HOA leads to the formation of an ammonium species, with the equilibrium of this reaction determined by the OcAm/HOA ratio and the temperature.<sup>37</sup> However, we did not find an influence of the amount of HOA or the ratio between HOA and OcAm on the optical properties of the obtained PbSe NPLs (see open and closed circle in Fig. 2b), and consider the role of the OcAm/HOA mixture is needed in our case to ensure dissolving of the precursors. Please note that a small amount of OcAm (167  $\mu\text{L}$ ) and HOA (19  $\mu\text{L}$ ) is always present during reaction due to the addition of the selenium precursor solution, and in the following description only additional amounts of OcAm and HOA added by the  $\text{Pb}(\text{OA})_2$  precursor solution is stated.

By plotting the excitonic absorption of the PbSe NPLs vs. their average edge length in Fig. 2a, we find the expected decreasing band gap energy with increasing NPL size.<sup>43</sup> The excitonic features of PbSe NPLs grow less distinct with increasing lateral NPL sizes due to an increased lateral size distribution, thus the 2<sup>nd</sup> derivative of the absorption was used for the plot as is described in the ESI (see Fig. S5†). Generally, an increase in the absorption width is found in larger NPLs as the absorption and PL is influenced by the lateral size of the NPLs rather than their thickness. We compare the obtained values with literature data for PbSe NCs expressed by an empirical sizing curve by Dai *et al.*<sup>44</sup> shown in Fig. 2a,

$$\Delta E = 4.41/(D_{\text{NCs}} + 0.51) \quad (1)$$

with  $D_{\text{NC}}$  as the average PbSe NC diameter, and  $\Delta E$  as the first excitonic absorption feature of the corresponding sample.

Clearly evident, we find the values for PbSe NPLs with a certain lateral size diverging toward higher energies than PbSe NCs with comparable diameters, which underpins the confinement in the thickness of the NPLs. The hyperbolic empirical fit for PbSe NCs is explained by the highly



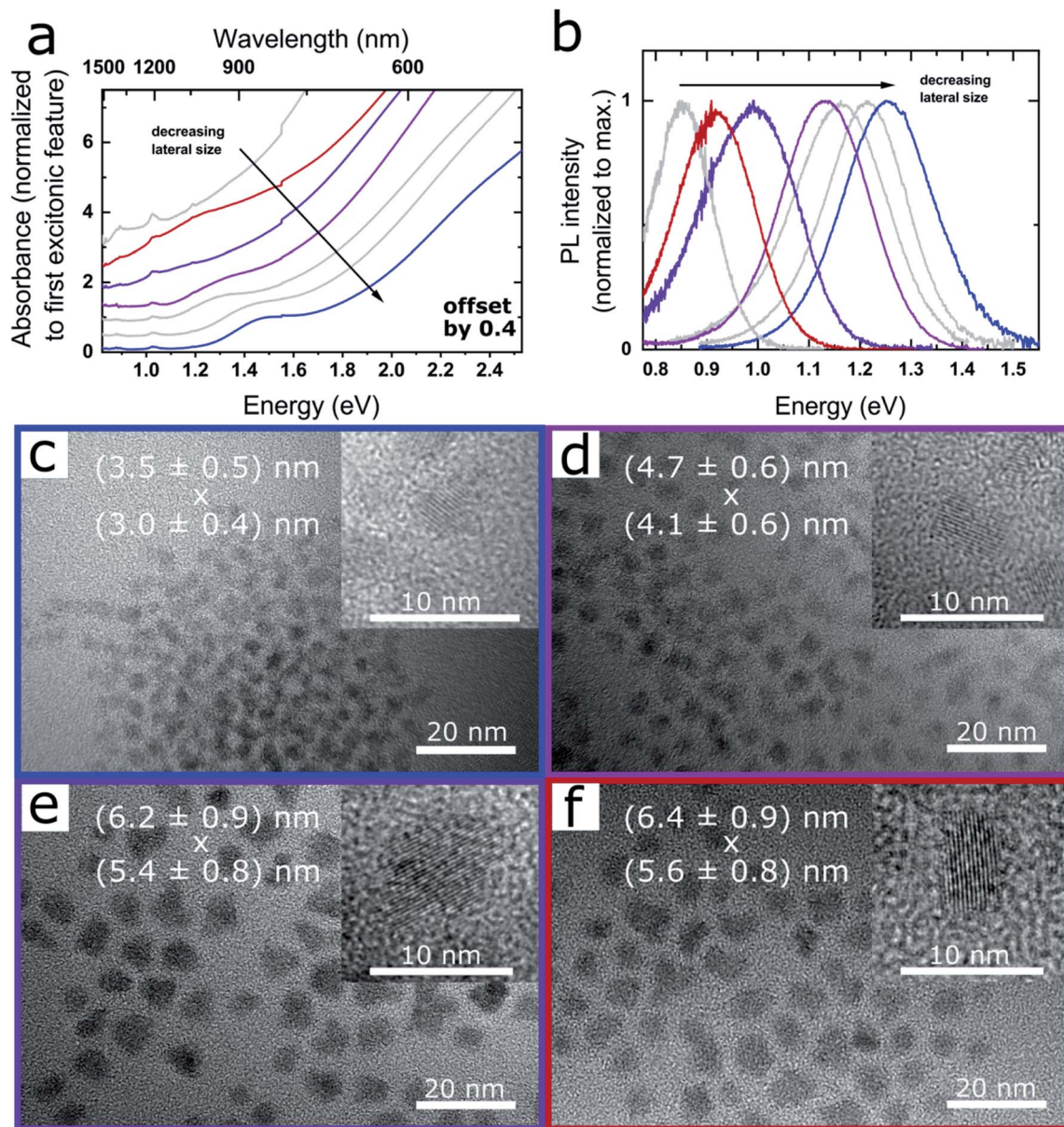


**Fig. 1** Optical properties and TEM images of CdCl<sub>2</sub> treated PbSe NPLs. (a) Absorbance, successive spectra are plotted with an offset of 0.4 for clarity and (b) associated PL of PbSe NPLs exhibiting excitonic features in the range of 800–1000 nm, and PL between 900–1450 nm. (c)–(f) TEM images of PbSe NPLs with associated absorption and PL shown in (a) and (b). The lateral size of the NPLs in x and y-direction is shown as overlay. PbSe NPLs exhibit a narrow lateral size distribution, with the inset showing single crystalline NPLs in high magnification. Corresponding data sets in (a) and (b) and TEM images are color-coded. Additional properties and reaction conditions for each sample are shown in Fig. 2 and listed in Table 1.

nonparabolic curvature of the conduction and valence band near the *L* point in lead chalcogenides and shows good agreement with both lead chalcogenide NCs and NPLs.<sup>3,44–47</sup>

We adopt a model by Kasowski *et al.*<sup>48</sup> and fit our data according to

$$\Delta E = (E_g^2 + 2\hbar^2 E_g (\pi/0.5 D_{\text{NPLs}})^2 / m^*)^{1/2} \quad (2)$$

with  $E_g$ , the bandgap of bulk PbSe (0.278 eV),<sup>49</sup>  $D_{\text{NPLs}}$  the average NPL edge length and  $m^*$  the effective mass of the charge carriers ( $m^* = m_e^* = m_h^*$ ). An effective mass of  $m^* = 0.060 \pm 0.002 m_e$  exhibits the best fit in good agreement with literature values for

PbSe NPLs reporting an effective mass of  $0.077 m_e$ .<sup>3</sup> The hyperbolic fit is given for both, 3D NCs and quantum wells in literature, allowing us to use the effective mass as the only variable in the Kasowski model and thus reducing the risk of overfitting.<sup>46,48</sup> While the lateral size of the PbSe NPLs is averaged over the width and length of the NPLs for this fit, we find the higher energy for the NPLs in comparison to spherical PbSe NCs of similar diameter also occurs when only plotting the longer or the shorter lateral edge length (see Fig. S6†).

While lateral confinement has been observed in CdSe and PbS NPLs,<sup>26,50,51</sup> its influence appears significantly higher in



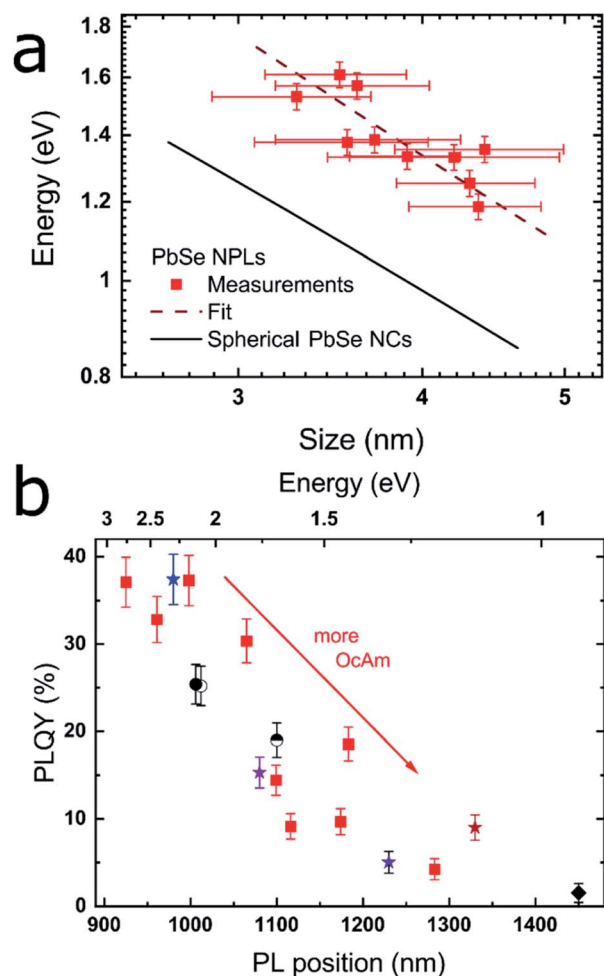


Fig. 2 Correlation between the band gap energy and lateral size of the PbSe NPLs, as well as between the PLQY and the PL maximum. (a) Position of the first excitonic transition vs. the lateral NPL size averaged over their  $x$ - and  $y$ -dimension as determined by the TEM images. The black line is an empirical fit for PbSe NCs published by Dai *et al.*,<sup>44</sup> while the dashed red line represents the fit to the PbSe NPLs which exhibit considerable additional confinement due to their 2D structure. (b) PLQY and PL position of different PbSe NPLs with red squares representing a reaction series with increasing OcAm amount, while retaining the total reaction volume as well as all other synthesis parameters. The results of the different synthesis conditions are represented by varying symbols and colors described in Table 1.

PbSe NPLs described here, which is shown in the NPL PL which is tunable over a large spectral range (see Fig. 1b) by a rather small lateral size increases of the NPLs. This originates from the larger exciton-Bohr-radius of PbSe (46 nm) in comparison to the exciton-Bohr-radii of PbS (23 nm) or CdSe (5.8 nm).<sup>52</sup>

Exemplary NPLs emitting at 1280 nm exhibit a thickness of  $0.8 \pm 0.1$  nm (Fig. S4†). This thickness corresponds to four atomic layers of cubic PbSe in the (100) direction. Note that the four monolayer definition of CdSe NPLs lacks application here. Zinc blende CdSe is structured by pure Cd and Se atomic layers and the term “4 ML” denotes four layers of Se and five layers of Cd, while a PbSe layer exhibits alternating Pb and Se atoms.

The PL maximum and the PLQY of CdCl<sub>2</sub> treated samples synthesized under different reaction conditions are shown in

Fig. 2b and summarized in Table 1. Low amounts of OcAm are sufficient for a successful synthesis and result in the formation of the smallest NPLs. While it is possible to obtain PbSe NPLs without OcAm addition to the Pb(OA)<sub>2</sub> precursor, we found the highest PLQY of 37.1% for NPLs with 0.2 mL OcAm added during the reaction (see Fig. 1c and 2b, blue star). The colored stars in Fig. 2b correspond to the samples shown in Fig. 1, with associated amounts of 0.2, 1.2, 1.4 and 1.9 mL OcAm present during reaction. With increasing amount of OcAm present in the reaction, the PLQY of PbSe NPLs drops and the absorption and PL exhibit a bathochromic shift (see Fig. 2b). We attribute the decrease in the PLQY of PbSe NPLs with a larger lateral size mainly to an “energy gap law” contribution, which has been described for organic dyes and lead chalcogenide NCs.<sup>53,54</sup> The reduced PLQY is explained by drastically faster non-radiative recombination rates in NPLs with a smaller band gap due to a decreased energy difference between trap states close to the conduction band and the band edge.<sup>54</sup>

We find the lowest temperature feasible for the NPL synthesis at  $-8$  °C since lower temperatures lead to freezing of the solvent. With temperatures at or slightly above room temperature, we obtain NPLs with excitonic absorption and emission reaching up to the telecommunication O-, E- and S-band. An example for an increase in reaction temperature with all other parameters kept constant is shown in Fig. 2b (blue star [0 °C] and semicircle [23 °C]). The PL maximum shifts bathochromically from 980 nm to 1100 nm with associated PLQY values of 37.4%, resp. 19.0%. We observe the same trend when increasing the OcAm amount in the synthesis indicating that higher PLQY values are correlated with a smaller lateral NPL size. PbSe NPLs with the smallest size (and size distribution) are obtained at reaction temperatures of 0 °C, which we kept as temperature for PbSe NPLs used in the benchmark experiments in this work.

### Postsynthetic CdCl<sub>2</sub> treatment and time-resolved spectroscopic investigation of PbSe NPLs

A drastic increase of the PbSe NPL PLQY is apparent after their postsynthetic treatment with CdCl<sub>2</sub>, which has been shown recently for NPLs and NCs.<sup>29,55–57</sup>

Table 1 PL maxima and reaction conditions for different PbSe NPL syntheses. The symbols correspond to the data shown in Fig. 2b with the first four rows corresponding to the PbSe NPLs discussed in Fig. 1

	PL maximum (nm)	PLQY (%)	OcAm (mL)	HOA (mL)	Hex (mL)	$T$ (°C)
★	980	37.4	0.2	0.4	1.8	0
★	1080	15.3	1.2	0.4	0.8	0
★	1230	5.0	1.4	0.4	0.6	23
★	1330	9.0	1.9	0.5	1.2	23
◆	1450	1.5	1.8	0.4	0.2	35
●	1100	19.0	0.2	0.4	1.8	23
○	1012	25.2	0.8	0.7	0.9	0
●	1006	25.4	0.8	0.1	1.5	0



We use ultrafast transient absorption spectroscopy (TAS) and multi-channel scaling (MCS) PL lifetime analysis for characterizing the photophysics and charge carrier dynamics of pristine and CdCl<sub>2</sub> treated PbSe NPLs. TA spectral and time traces of PbSe NPLs with PL centered at 985 nm (1.3 eV, pristine) and 1050 nm (1.2 eV, CdCl<sub>2</sub> treated) are exemplarily shown in Fig. 3. We exclude the formation of an alloy or CdSe shell growth on PbSe NPLs during the metal halide treatment since reaction temperatures of 0 °C and room temperature are rather low (see Fig. 4a for comparison).<sup>57,58</sup>

PbSe NPL samples were photoexcited at 700 nm (with an optical density of sample solutions of  $\leq 0.1$ ) and with comparable photoexcitation fluence ( $30 \mu\text{J cm}^{-2}$ ) to ensure a similar distribution of the number of photoexcited excitons in pristine and CdCl<sub>2</sub> treated PbSe NPL samples.<sup>29</sup> TA spectral line cuts at 10 ps after photoexcitation shown in Fig. 3a exhibit a prominent ground state bleach (GSB) feature due to state filling and stimulated emission centered at 880 nm for the pristine, and 950 nm for the CdCl<sub>2</sub> treated NPLs, respectively.<sup>59</sup> Generally, the

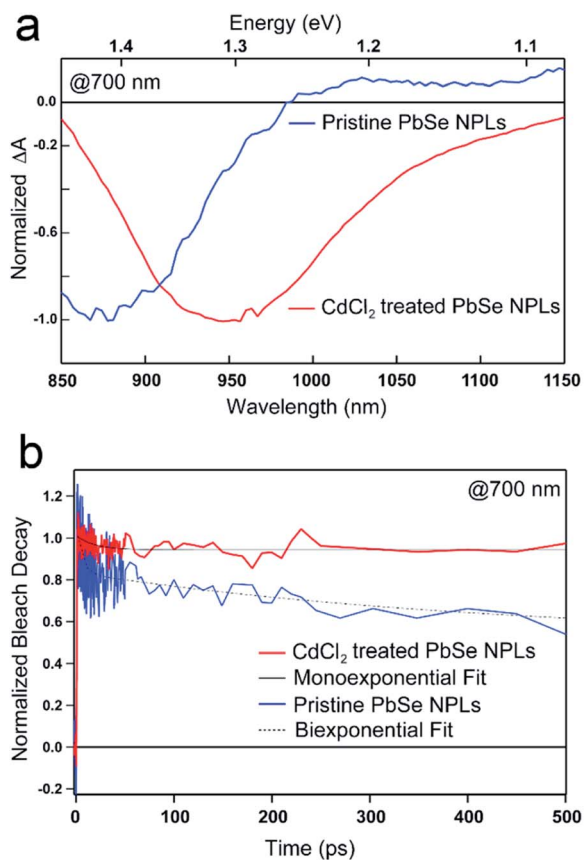


**Fig. 3** TA spectra of PbSe NPLs emitting at 985 nm and 1050 nm, resp. and photoexcited at 700 nm. (a) Spectral line cuts of pristine (blue) and CdCl<sub>2</sub> treated (red) PbSe NPLs at a delay time of 10 ps after photoexcitation with the samples exhibiting a prominent bleach feature at 880 nm (pristine) and 950 nm (CdCl<sub>2</sub> treated), resp. (b) Exciton dynamics of the pristine (blue) and CdCl<sub>2</sub> treated (red) PbSe NPLs show a decay over the course of the measurement with transients of the pristine samples decaying biexponentially, while CdCl<sub>2</sub> treated samples exhibit single exponential decay dynamics.

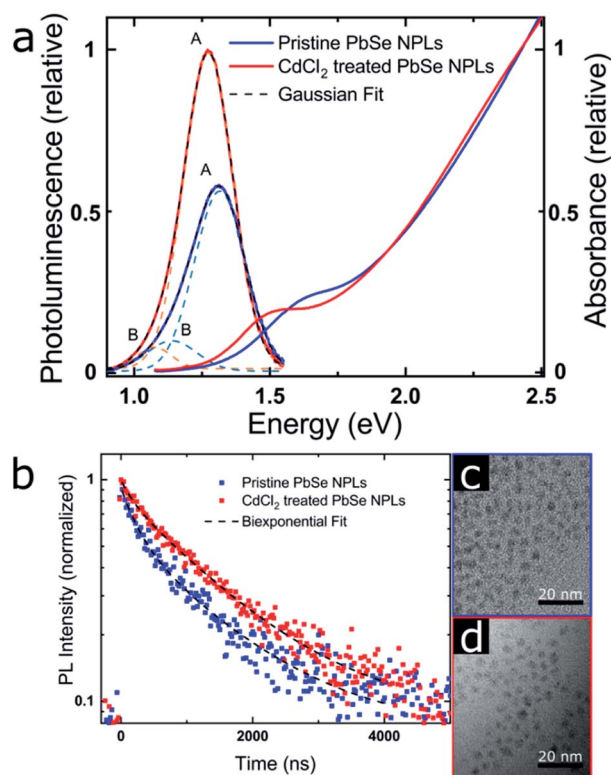


**Fig. 4** PbSe NPL PL properties (emitting at 940 nm [pristine] and 980 nm [CdCl<sub>2</sub> treated]) (a) PL and absorbance. The PL data was corrected for the transformation from the wavelength to the energy scale by a Jacobian transformation.<sup>69</sup> The dashed lines represent a fit of the PL with the sum of two Gaussian. (b) MCS PL lifetime measurements, taken at each PL maximum and exhibiting a biexponential decay with increasing contribution of the longer lifetime after the CdCl<sub>2</sub> treatment. (c) and (d) TEM images of the pristine and CdCl<sub>2</sub> treated NPLs showing a slight NPL size increase after the treatment.

GSB of PbSe NPLs is slightly blue-shifted with respect to the steady-state absorption by a biexcitonic shift.<sup>59</sup> Due to the initial fast cooling of hot charges (photoexcitation at 700 nm, above the NPL band edge, see Fig. S7† for absorption and Fig. S8† for color-coded 2D spectra), a short-lived induced absorption is probed, which decays within the first 2 ps of the measurement. After the CdCl<sub>2</sub> treatment, the GSB of PbSe NPLs is red-shifted by 70 nm (100 meV) and hence following the same trend as the steady-state absorption and emission of the NPLs. Spectral line cuts taken at short (1 ps) and longer (3.5 ns) times after photoexcitation (Fig. S9†) underpin changes in the GSB feature of PbSe NPLs mainly at their emission wavelengths (985 nm and 1050 nm) over the course of the measurement. We find the bleach contribution of pristine PbSe NPLs at 985 nm to have significantly decayed after 3.5 ns, while CdCl<sub>2</sub> treated samples still exhibit a considerably higher contribution at 1050 nm after 3.5 ns. This is in good agreement with the measured significantly higher PLQY values of CdCl<sub>2</sub> treated samples (2.3% prior to and 35.3% after the treatment). Fig. 3b depicts the exciton decay dynamics of PbSe NPLs with the GSB features of pristine and CdCl<sub>2</sub> treated PbSe NPLs being long-lived generally (exceeding the measurement time window of 6 ns, Fig. S8†),



which is well in accordance with the PLQY found for both samples. Decay dynamics of photoexcited pristine PbSe NPLs are fitted biexponentially ( $\tau_{1\text{bleach}} = 5.5 \pm 1.5$  ps,  $\tau_{2\text{bleach}} = 400 \pm 160$  ps), while CdCl<sub>2</sub> treated samples can be described with a single exponential decay ( $\tau_{1\text{bleach}} = 19 \pm 4$  ps). Although the ultrafast exciton decay dynamics of PbSe NPLs shown in Fig. 3b lack direct comparability with the PL lifetime measurements carried out (ps to ns timescales considered by TAS in comparison to tens of ns to  $\mu$ s timescales considered by time-resolved PL), they underpin that already at ultrafast time scales (1 ps to 6 ns), the contribution of multiple relaxation pathways gets apparent in pristine PbSe NPLs (see Fig. 3b), while one relaxation pathway seems to be effective in CdCl<sub>2</sub> treated PbSe NPLs at early times after photoexcitation.

### PL contributions

The absorption and PL spectra of PbSe NPLs and associated TEM images before and after the CdCl<sub>2</sub> treatment are shown in Fig. 4 (size histograms in Fig. S10†). We find two components contributing to the PL lifetime, which is apparent from the slightly asymmetric shape of the PbSe NPL PL (Fig. 4a) and has been described for PbS and PbSe NCs.<sup>60,61</sup> We fit the PL spectra with the sum of two Gaussian<sup>29,62,63</sup> and the Gaussian centered at higher energy (labeled A) is ascribed to the PbSe band gap associated PL, while the lower energy PL (labeled B) is related to surface traps.<sup>63</sup>

The PL lifetimes of PbSe NPLs (Fig. 4b and Table 2) are fitted biexponentially with the same time constants  $\tau_{1\text{PL}} = 168$  ns and  $\tau_{2\text{PL}} = 1320$  ns. These values are slightly longer than lifetimes typically found for PbSe NCs ( $\sim 100$ – $1000$  ns) but shorter than lifetimes measured for PbSe NPLs synthesized by cation exchange and comparable thickness (0.7–2.7  $\mu$ s).<sup>20,64–66</sup> For fitting the data, the PL lifetime of the CdCl<sub>2</sub> treated PbSe NPLs was run freely, and the pristine sample was fitted using fixed lifetime parameters with both components exhibiting good residual ( $R^2 = 0.98$  and  $R^2 = 0.97$ , resp.). After the CdCl<sub>2</sub> treatment however, we find the contribution of the faster time constant significantly reduced from 40% to 15% (Table 2), associated with an increase of the slower time constant to 85% (Table 2). We assign these contributions to two radiative processes present in the PbSe NPL PL, with the faster time constant related to surface trap state emission and the slower time constant related to exciton recombination. The decrease of the contribution of  $\tau_{1\text{PL}}$  leads to an increase in the PL lifetime and PLQY of the PbSe NPLs, rendering the CdCl<sub>2</sub> surface treatment successful in fixing surface-related trap states.<sup>54,67</sup> To assign the time constants extracted from the PL lifetime measurements to their respective PL contribution, we

exemplary determine the PL lifetimes at the maxima of each Gaussian fitted (see Fig. S11 and Table S1†) and find a biexponential decay, with different contributions of the two constants to the respective PL decay. The shorter PL lifetime constant ( $\tau_{1\text{PL}} = 168$  ns) shows higher contribution at the maximum of peak B and is thus assigned to the trap state related emission, while the longer PL lifetime constant ( $\tau_{2\text{PL}} = 1320$  ns) is dominant at peak A and is assigned to the excitonic emission. Even for pristine PbSe NPLs, the trap state emission shows a small contribution, while the PL is dominated by the band gap transition (ratio A : B 6.5 : 1). After the CdCl<sub>2</sub> treatment, this effect is further enhanced as is shown by the peak area ratio of feature A (ratio A : B increasing to 22 : 1, see Table 3). The FWHM of the excitonic PL peak A decreases slightly from 221 to 214 meV after the CdCl<sub>2</sub> treatment, while the FWHM of the PL peak B is significantly reduced from 217 meV to 149 meV (Fig. 4a) further underpinning the positive effect of the CdCl<sub>2</sub> treatment. All PbSe NPL samples synthesized in this work follow this trend, and a FWHM of 180–220 meV is representative for the NPL PL, independent of the respective PL maximum (Table S2†). The FWHM of PbSe NPLs synthesized here are slightly broader than FWHM typically obtained for PbSe NCs (50–150 meV) that exhibit a band gap below 1.5 eV as well as PbSe NPLs synthesized by cation exchange (PL at 0.93 eV, FWHM of 116 meV for contribution A).<sup>20,63,68</sup> We attribute the PL FWHM values of the PbSe NPLs shown here mainly to their lateral size distribution. However, PbS and PbSe NCs generally exhibit tunable emission with decreasing PLQY values for increasing NC sizes.<sup>68</sup> For example, while the PLQY for small PbSe NCs with a band gap > 1.3 eV reaches 60%, NCs with a band gap < 1.2 eV have a PLQY of less than 40%.<sup>54,68</sup> This renders our PbSe NPLs superior at shorter wavelengths (higher energy) where their PLQY values match or even exceed the PLQY of small PbSe NCs.

TEM images shown in Fig. 4c and d (as well as Fig. 1) underpin the lack of a NPL shape transformation upon CdCl<sub>2</sub> treatment. A small lateral size increase (from  $3.6 \times 3.1$  nm<sup>2</sup> to  $4.2 \times 3.5$  nm<sup>2</sup>) is apparent, which is also shown in the redshift of the NPL absorption after the treatment. The slight increase in lateral size assumedly originates from the additional reaction time after the CdCl<sub>2</sub> treatment of the pristine NPLs. However, a change in the thickness of the NPLs or a release of lattice strain by the CdCl<sub>2</sub> treatment cannot be ruled out completely and has been *e.g.* observed for CdSe NPLs.<sup>70–72</sup> The CdCl<sub>2</sub> treatment of PbSe NPLs is accompanied by a significant increase of the PLQY with the highest value determined for NPLs with an emission maximum of 1.27 eV (980 nm) from

**Table 2** PL lifetimes of pristine and CdCl<sub>2</sub> treated PbSe NPLs (emitting at 940 nm and 980 nm, resp.)

PbSe NPLs	$\tau_{1\text{PL}}$ (ns)	$A_1$ (%)	$\tau_{2\text{PL}}$ (ns)	$A_2$ (%)
	Pristine	168	40	1320
CdCl <sub>2</sub> treated	168	15	1320	85

**Table 3** Values for the two Gaussian of pristine and CdCl<sub>2</sub> treated PbSe NPLs (emitting at 940 nm and 980 nm, resp.)

PbSe NPLs	Peak center (eV)		FWHM (meV)		Peak area		Peak ratio
	A	B	A	B	A	B	A : B
Pristine	1.32	1.14	221	217	0.13	0.02	6.5
CdCl <sub>2</sub> treated	1.27	1.07	214	149	0.22	0.01	22.0



14.7% before to 37.4%. Excitation spectra shown in Fig. S12<sup>†</sup> additionally support the absence of a contribution of spherical PbSe NCs as side products in the synthesis to the NPL PL. To assess the impact of the CdCl<sub>2</sub> treatment on the PbS NPL surface, the relationship between the PLQY and the trap state density is considered as inversely linear, *i.e.* halving the trap state density results in a doubling of the PLQY.<sup>55,73</sup> We conclude that nearly half of the initial surface traps in pristine PbSe NPLs emitting at 1.27 eV (980 nm) are saturated by the CdCl<sub>2</sub> treatment. As described in the discussion of Fig. 2b, an explanation for the decreased PLQY in larger PbSe NPLs with smaller band gaps is given by the “energy gap law” contribution, leading to increased non-radiative recombination rates due to a decreased trap state and band edge energy difference.<sup>53,54</sup> This contribution has to be considered for the CdCl<sub>2</sub> treatment and PLQY of larger PbSe NPLs.

The chemical composition of the PbSe NPLs was determined by EDXS (see Table S3<sup>†</sup>). We find that the NPLs exhibit a slight Pb excess before and after the CdCl<sub>2</sub> treatment, which is typical for PbSe NCs (Pb : Se ratio 1.2 : 1).<sup>74</sup> The optical properties of PbSe NPLs shown in Fig. 4c and d only indicate small changes in the NPL lateral size, which is supported by the TEM images. Furthermore, after the CdCl<sub>2</sub> treatment EDXS results show a Cd : Cl ratio of 1.8 : 1, closely resembling the molecular composition of CdCl<sub>2</sub>. This indicates CdCl<sub>2</sub> acting as Z-type ligand for stabilizing PbSe NPLs.<sup>43</sup> However, chloride anions could also act as X-type ligands, providing charge neutrality to the NPLs.<sup>55,56</sup>

## Conclusions

In conclusion, we have shown the first low temperature direct colloidal synthesis of PbSe NPLs with distinct excitonic absorption features in the range of 1.55–1.24 eV (800–1000 nm). The optical properties of the NPLs are tuned by controlling their lateral dimension with the addition of octylamine and the reaction temperature, with increasing octylamine amount and higher reaction temperatures yielding larger NPLs. An efficient infrared PL of PbSe NPLs with QY values of up to 37.4% between 1.38–0.86 eV (900–1450 nm) is obtained by their postsynthetic treatment with CdCl<sub>2</sub>. Transient absorption and time-resolved PL spectroscopy reveal a considerable decrease of surface related trap states and non-radiative recombination in the PbSe NPLs by the treatment, rendering them efficient colloidal quantum emitters at telecommunication wavelengths.

## Conflicts of interest

There are no conflicts to declare.

## Acknowledgements

J. H. gratefully acknowledges financial support by the Deutsche Forschungsgemeinschaft (DFG, German Research Foundation) under Germany's Excellence Strategy -EXC-2123 Quantum-Frontiers - 390837967 and HU 1318/4-1. L. K., L. B. and J. L. gratefully acknowledge funding by the Deutsche

Forschungsgemeinschaft (DFG, German Research Foundation) under Germany's Excellence Strategy within the Cluster of Excellence PhoenixD (EXC 2122, Project ID 390833453). J. L. is thankful for additional funding by the Caroline Herschel program of the Leibniz Universität Hannover. The authors thank the Laboratory for Nano and Quantum Engineering (LNQE) in Hannover for access to the TEM. We thank Nadja C. Bigall for access to the photoluminescence spectrometer and Dirk Dorfs for access to the UV-Vis-NIR absorption spectrometer. We are grateful to Armin Feldhoff for providing the XRD facilities.

## Notes and references

- C. Schliehe, B. H. Juarez, M. Pelletier, S. Jander, D. Greshnykh, M. Nagel, A. Meyer, S. Foerster, A. Kornowski, C. Klinke and H. Weller, *Science*, 2010, **329**, 550–553.
- Q. A. Akkerman, B. Martín-García, J. Buha, G. Almeida, S. Toso, S. Marras, F. Bonaccorso, U. Petralanda, I. Infante and L. Manna, *Chem. Mater.*, 2019, **31**, 8145–8153.
- W.-K. Koh, N. K. Dandu, A. F. Fidler, V. I. Klimov, J. M. Pietryga and S. V. Kilina, *J. Am. Chem. Soc.*, 2017, **139**, 2152–2155.
- Z. Jiang, G. B. Bhandari, S. M. Premathilaka, S. Khan, D. M. Dimick, C. Stombaugh, A. Mandell, Y. He, H. Peter Lu and L. Sun, *Phys. Chem. Chem. Phys.*, 2015, **17**, 23303–23307.
- K. D. Desmet, D. A. Paz, J. J. Corry, J. T. Eells, M. T. T. Wong-Riley, M. M. Henry, E. V. Buchmann, M. P. Connelly, J. V. Dovi, H. L. Liang, D. S. Henshel, R. L. Yeager, D. S. Millsap, J. Lim, L. J. Gould, R. Das, M. Jett, B. D. Hodgson, D. Margolis and H. T. Whelan, *Photomed. Laser Surg.*, 2006, **24**, 121–128.
- F. Koch, S. V. Chernikov and J. R. Taylor, *Opt. Commun.*, 2000, **175**, 209–213.
- M. M. R. Moayed, T. Bielewicz, M. S. Zoellner, C. Herrmann and C. Klinke, *Adv. Photonics*, 2017, DOI: 10.1364/noma.2017.NoTu1C.3.
- M. Aerts, T. Bielewicz, C. Klinke, F. C. Grozema, A. J. Houtepen, J. M. Schins and L. D. A. Siebbeles, *Nat. Commun.*, 2014, **5**, 3789.
- S. Dogan, T. Bielewicz, Y. Cai and C. Klinke, *Appl. Phys. Lett.*, 2012, **101**, 73102.
- J. Lauth, M. Failla, E. Klein, C. Klinke, S. Kinge and L. D. A. Siebbeles, *Nanoscale*, 2019, **11**, 21569–21576.
- T. Bielewicz, S. Dogan and C. Klinke, *Small*, 2015, **11**, 826–833.
- Z. Chen, B. Nadal, B. Mahler, H. Aubin and B. Dubertret, *Adv. Funct. Mater.*, 2014, **24**, 295–302.
- M. Bernardi, M. Palummo and J. C. Grossman, *Nano Lett.*, 2013, **13**, 3664–3670.
- S. Dogan, T. Bielewicz, V. Lebedeva and C. Klinke, *Nanoscale*, 2015, **7**, 4875–4883.
- S. Krishnamurthy, A. Singh, Z. Hu, A. V. Blake, Y. Kim, A. Singh, E. A. Dolgoplova, D. J. Williams, A. Piryatinski,





- A. V. Malko, H. Htoon, M. Sykora and J. A. Hollingsworth, *ACS Nano*, 2021, **15**, 575–587.
- 16 C. J. Hanson, N. F. Hartmann, A. Singh, X. Ma, W. J. I. DeBenedetti, J. L. Casson, J. K. Grey, Y. J. Chabal, A. V. Malko, M. Sykora, A. Piryatinski, H. Htoon and J. A. Hollingsworth, *J. Am. Chem. Soc.*, 2017, **139**, 11081–11088.
- 17 F. Xu, X. Ma, Q. Zhang, H.-K. Lo and J.-W. Pan, *Rev. Mod. Phys.*, 2020, **92**(2), 025002.
- 18 X. Cao, M. Zopf and F. Ding, *J. Semicond.*, 2019, **40**, 71901.
- 19 S. M. Tenney, V. Vilchez, M. L. Sonnleitner, C. Huang, H. C. Friedman, A. J. Shin, T. L. Atallah, A. P. Deshmukh, S. Ithurria and J. R. Caram, *J. Phys. Chem. Lett.*, 2020, **11**, 3473–3480.
- 20 T. Galle, M. Samadi Khoshkhou, B. Martin-Garcia, C. Meerbach, V. Sayevich, A. Koitzsch, V. Lesnyak and A. Eychmüller, *Chem. Mater.*, 2019, **31**, 3803–3811.
- 21 T. Galle, D. Spittel, N. Weiß, V. Shamraienko, H. Decker, M. Georgi, R. Hübner, N. Metzkwow, C. Steinbach, D. Schwarz, V. Lesnyak and A. Eychmüller, *J. Phys. Chem. Lett.*, 2021, **12**, 5214–5220.
- 22 S. Ithurria, M. D. Tessier, B. Mahler, R. P. S. M. Lobo, B. Dubertret and A. L. Efros, *Nat. Mater.*, 2011, **10**, 936–941.
- 23 A. D. Antu, Z. Jiang, S. M. Premathilka, Y. Tang, J. Hu, A. Roy and L. Sun, *Chem. Mater.*, 2018, **30**, 3697–3703.
- 24 H. Zhang, B. H. Savitzky, J. Yang, J. T. Newman, K. A. Perez, B.-R. Hyun, L. F. Kourkoutis, T. Hanrath and F. W. Wise, *Chem. Mater.*, 2016, **28**, 127–134.
- 25 D. D. Vaughn, R. J. Patel, M. A. Hickner and R. E. Schaak, *J. Am. Chem. Soc.*, 2010, **132**, 15170–15172.
- 26 P. J. Morrison, R. A. Loomis and W. E. Buhro, *Chem. Mater.*, 2014, **26**, 5012–5019.
- 27 A. H. Khan, S. Pal, A. Dalui, J. Pradhan, D. D. Sarma and S. Acharya, *Chem. Mater.*, 2017, **29**, 1175–1182.
- 28 A. H. Khan, R. Brescia, A. Polovitsyn, I. Angeloni, B. Martín-García and I. Moreels, *Chem. Mater.*, 2017, **29**, 2883–2889.
- 29 F. Manteiga Vázquez, Q. Yu, L. F. Klepzig, L. D. A. Siebbeles, R. W. Crisp and J. Lauth, *J. Phys. Chem. Lett.*, 2021, **12**, 680–685.
- 30 Y. Chen, D. Chen, Z. Li and X. Peng, *J. Am. Chem. Soc.*, 2017, **139**, 10009–10019.
- 31 Y. Zhou, M. Celikin, A. Camellini, G. Sirigu, X. Tong, L. Jin, K. Basu, D. Barba, D. Ma, S. Sun, F. Vidal, M. Zavelani-Rossi, Z. M. Wang, H. Zhao, A. Vomiero and F. Rosei, *Adv. Energy Mater.*, 2017, **7**, 1602728.
- 32 Y.-H. Liu, F. Wang, Y. Wang, P. C. Gibbons and W. E. Buhro, *J. Am. Chem. Soc.*, 2011, **133**, 17005–17013.
- 33 J. S. Son, X.-D. Wen, J. Joo, J. Chae, S.-I. Baek, K. Park, J. H. Kim, K. An, J. H. Yu, S. G. Kwon, S.-H. Choi, Z. Wang, Y.-W. Kim, Y. Kuk, R. Hoffmann and T. Hyeon, *Angew. Chem., Int. Ed.*, 2009, **48**, 6861–6864.
- 34 A. Riedinger, F. D. Ott, A. Mule, S. Mazzotti, P. N. Knüsel, S. J. Kress, F. Prins, S. C. Erwin and D. J. Norris, *Nat. Mater.*, 2017, **16**, 743–748.
- 35 M. P. Campos, M. P. Hendricks, A. N. Beecher, W. Walravens, R. A. Swain, G. T. Cleveland, Z. Hens, M. Y. Sfeir and J. S. Owen, *J. Am. Chem. Soc.*, 2017, **139**, 2296–2305.
- 36 J. S. Owen, E. M. Chan, H. Liu and A. P. Alivisatos, *J. Am. Chem. Soc.*, 2010, **132**, 18206–18213.
- 37 G. Almeida, L. Goldoni, Q. Akkerman, Z. Dang, A. H. Khan, S. Marras, I. Moreels and L. Manna, *ACS Nano*, 2018, **12**, 1704–1711.
- 38 M. P. Hendricks, M. P. Campos, G. T. Cleveland, I. Jen-La Plante and J. S. Owen, *Science*, 2015, **348**, 1226–1230.
- 39 J. Lauth, G. Grimaldi, S. Kinge, A. J. Houtepen, L. D. A. Siebbeles and M. Scheele, *Angew. Chem., Int. Ed.*, 2017, **56**, 14061–14065.
- 40 F. C. M. Spoor, L. T. Kunneman, W. H. Evers, N. Renaud, F. C. Grozema, A. J. Houtepen and L. D. A. Siebbeles, *ACS Nano*, 2016, **10**, 695–703.
- 41 J. A. McGuire, J. Joo, J. M. Pietryga, R. D. Schaller and V. I. Klimov, *Acc. Chem. Res.*, 2008, **41**, 1810–1819.
- 42 Y. Wang, Y. Zhou, Y. Zhang and W. E. Buhro, *Inorg. Chem.*, 2015, **54**, 1165–1177.
- 43 A. I. Ekimov and A. A. Onushchenko, *JETP Lett.*, 1981, **34**, 345–348.
- 44 Q. Dai, Y. Wang, X. Li, Y. Zhang, D. J. Pellegrino, M. Zhao, B. Zou, J. Seo, Y. Wang and W. W. Yu, *ACS Nano*, 2009, **3**, 1518–1524.
- 45 I. Kang and F. W. Wise, *J. Opt. Soc. Am. B*, 1997, **14**, 1632.
- 46 G. Allan and C. Delerue, *Mater. Sci. Eng., C*, 2005, **25**, 687–690.
- 47 F. C. M. Spoor, G. Grimaldi, C. Delerue, W. H. Evers, R. W. Crisp, P. Geiregat, Z. Hens, A. J. Houtepen and L. D. A. Siebbeles, *ACS Nano*, 2018, **12**, 4796–4802.
- 48 Y. Wang, A. Suna, W. Mahler and R. Kasowski, *J. Chem. Phys.*, 1987, **87**, 7315–7322.
- 49 In *Non-Tetrahedrally Bonded Elements and Binary Compounds I*, O. Madelung, U. Rössler and M. Schulz, Springer-Verlag, Berlin/Heidelberg, 1998, pp. 1–8.
- 50 S. Ithurria, G. Bousquet and B. Dubertret, *J. Am. Chem. Soc.*, 2011, **133**, 3070–3077.
- 51 G. H. V. Bertrand, A. Polovitsyn, S. Christodoulou, A. H. Khan and I. Moreels, *Chem. Commun.*, 2016, **52**, 11975–11978.
- 52 L. Brus, *J. Phys. Chem.*, 1986, **90**, 2555–2560.
- 53 H. C. Friedman, E. D. Cosco, T. L. Atallah, S. Jia, E. M. Sletten and J. R. Caram, *Chem*, 2021, **7**(12), 3359–3376.
- 54 O. E. Semonin, J. C. Johnson, J. M. Luther, A. G. Midgett, A. J. Nozik and M. C. Beard, *J. Phys. Chem. Lett.*, 2010, **1**, 2445–2450.
- 55 N. Kirkwood, J. O. V. Monchen, R. W. Crisp, G. Grimaldi, H. A. C. Bergstein, I. Du Fossé, W. van der Stam, I. Infante and A. J. Houtepen, *J. Am. Chem. Soc.*, 2018, **140**, 15712–15723.
- 56 M. Dufour, J. Qu, C. Greboval, C. Méthivier, E. Lhuillier and S. Ithurria, *ACS Nano*, 2019, **13**, 5326–5334.
- 57 W. K. Bae, J. Joo, L. A. Padilha, J. Won, D. C. Lee, Q. Lin, W.-K. Koh, H. Luo, V. I. Klimov and J. M. Pietryga, *J. Am. Chem. Soc.*, 2012, **134**, 20160–20168.
- 58 P. B. Green, Z. Li and M. W. Wilson, *J. Phys. Chem. Lett.*, 2019, **10**, 5897–5901.



- 59 J. M. Schins, M. T. Trinh, A. J. Houtepen and L. D. A. Siebbeles, *Phys. Rev. B: Condens. Matter Mater. Phys.*, 2009, **80**(3), 03523.
- 60 J. M. Harbold and F. W. Wise, *Phys. Rev. B: Condens. Matter Mater. Phys.*, 2007, **76**(12), 125304.
- 61 J. R. Caram, S. N. Bertram, H. Utzat, W. R. Hess, J. A. Carr, T. S. Bischof, A. P. Beyler, M. W. B. Wilson and M. G. Bawendi, *Nano Lett.*, 2016, **16**, 6070–6077.
- 62 O. Erdem, M. Olutas, B. Guzelturk, Y. Kelestemur and H. V. Demir, *J. Phys. Chem. Lett.*, 2016, **7**, 548–554.
- 63 I. Skurlov, A. Sokolova, T. Galle, S. Cherevko, E. Ushakova, A. Baranov, V. Lesnyak, A. Fedorov and A. Litvin, *Nanomaterials*, 2020, **10**(12), 2570.
- 64 J. M. An, A. Franceschetti and A. Zunger, *Nano Lett.*, 2007, **7**, 2129–2135.
- 65 M. Sykora, A. Y. Kuposov, J. A. McGuire, R. K. Schulze, O. Tretiak, J. M. Pietryga and V. I. Klimov, *ACS Nano*, 2010, **4**, 2021–2034.
- 66 A. Kigel, M. Brumer, G. I. Maikov, A. Sashchiuk and E. Lifshitz, *Small*, 2009, **5**, 1675–1681.
- 67 B. R. Fisher, H.-J. Eisler, N. E. Stott and M. G. Bawendi, *J. Phys. Chem. B*, 2004, **108**, 143–148.
- 68 H. Lu, G. M. Carroll, N. R. Neale and M. C. Beard, *ACS Nano*, 2019, **13**, 939–953.
- 69 J. Mooney and P. Kambhampati, *J. Phys. Chem. Lett.*, 2013, **4**, 3316–3318.
- 70 N. Moghaddam, C. Dabard, M. Dufour, H. Po, X. Xu, T. Pons, E. Lhuillier and S. Ithurria, *J. Am. Chem. Soc.*, 2021, **143**, 1863–1872.
- 71 S. Christodoulou, J. I. Climente, J. Planelles, R. Brescia, M. Prato, B. Martín-García, A. H. Khan and I. Moreels, *Nano Lett.*, 2018, **18**, 6248–6254.
- 72 C. Meerbach, C. Wu, S. C. Erwin, Z. Dang, A. Prudnikau and V. Lesnyak, *Chem. Mater.*, 2020, **32**, 566–574.
- 73 C. Bullen and P. Mulvaney, *Langmuir*, 2006, **22**, 3007–3013.
- 74 M. C. Weidman, M. E. Beck, R. S. Hoffman, F. Prins and W. A. Tisdale, *ACS Nano*, 2014, **8**, 6363–6371.

